Micromechanics Digital Rock: Parameterization of Consolidation Level using a Grain Contact Model

Zhuang Sun*, *Rafael* Salazar-Tio, *Andrew* Fager, and *Bernd* Crouse

Dassault Systèmes, 343 Sansome St San Francisco, CA, USA

Abstract. The mechanical behaviour of sedimentary rocks is conditioned by the interactions at the grain-grain contacts. We present a micromechanics digital rock workflow based on a cohesive contact model and introduce a general parameterization that can capture two extreme contact behaviours: free grains and fixed grains, as well as any intermediate degree of grain consolidation. With this parametric cohesive contact model, we can simulate a wide range of sedimentary rocks, from unconsolidated to well-consolidated rocks. We present a benchmark study on several samples and compare with laboratory-measured elastic moduli to calibrate its degree of consolidation. Simulations that do not include the grain contact modelling, tend to overestimate the elastic moduli, which manifests the significance of this contribution to capture well the grain contact behaviour. To demonstrate the impact of properly capturing the degree of consolidation on the rock strength and failure pattern, we present results for numerical uniaxial compression testing. This workflow provides physics-based solution to complex grain contact behaviour, which complements laboratory core analysis, and can be useful to reveal underlying grain-scale processes governing rock mechanical behaviour.

1 Introduction

Digital rock applications have rapidly emerged over the past decades based on X-ray micro-tomography (micro-CT) imaging technology that allows capturing pore-scale three-dimensional (3D) structures of reservoir rocks at the micro-meter scale, and virtually simulating the flow of fluids under different production conditions [1–9]. However, digital rock simulation of rock mechanical properties has been considered challenging given the intrinsic limitation of micro-CT images to capture the degree of consolidation between grains in rocks, due to the limit in imaging resolution and also because micro-CT is typically obtained at ambient conditions and does not capture the actual net confining stress (NCS) pore geometry [10–15].

Different levels of consolidation, compaction, recrystallization, and diagenesis in general, can produce a wide range of grain contact behaviours in sedimentary rocks, from loosely consolidated sand packs to completely fused grains that form a single solid structure [16]. Numerical methods in the literature typically use a single solid frame formed by the mineral grains, generally overestimating the simulated rock stiffness as compared to experimental measurements [2,10,17–19]. Some ideas have been discussed to assign different properties to contact regions and grain regions [20–22]. However, a commonality among these approaches is that grain relocation is not allowed, which limits the grain-grain contact behaviour of real rocks as well as rock failure significant deformation.

We recently introduced a micromechanics digital rock workflow based on finite element modelling of grain structures obtained from micro-CT images [23]. Some unique features of this workflow include, a robust grain-grain segmentation method, a conformal grain-grain contact meshing algorithm, and grain relocation capabilities, instead of modelling a solid framework as a whole. We are able to simulate linear elastic moduli comparable with experimental values, as well as being able to simulate significant compaction found at in-situ conditions, which are difficult to capture using micro-CT imaging at ambient conditions.

Here we present an extension of that work, based on a cohesive contact model and we introduce a general parameterization that can capture both extreme contact behaviours: free grains and fixed grains, as well as an intermediate degree of grain consolidation. The proposed workflow intends to solve problems including: (1) model properly variable grain-grain consolidation to correctly simulate mechanical rock properties, (2) being able to recover the correct NCS pore geometry to simulate all petrophysical properties under the correct in-situ conditions, (3) allow grain relocation capabilities, including failure test simulations. This paper is structured as follows. First, we describe the parametric cohesive contact model to simulate a wide range of sedimentary rocks, from unconsolidated to well-consolidated rocks. Second, we show a benchmark study on sandstone samples and compare with laboratory-measured elastic moduli to calibrate its degree of consolidation. Finally, we perform numerically uniaxial compression tests to demonstrate the impact of properly capturing the degree of consolidation on the rock strength and failure pattern.

2 Methodology

A micro-CT 3D voxelized image is needed as an input to identify individual grains and a connected pore geometry of rock. The limitations of micro-CT images for properly capturing a micro-mechanics rock model are related to the insufficient contrast for the identification of different mineral

* Corresponding author: zhuang.sun@3ds.com

grains, and for the identification of grain-grain contacts between same mineral grains. Identification of grain mineralogy and contacts can be improved by complementing 3D micro-CT imaging with 2D higher resolution and mineralogy imaging such as scanning electron microscopy (SEM) and energy dispersive x-ray spectroscopy (EDS). In order to setup a finite element (FE) micro-mechanics rock model from micro-CT data, two critical pre-processing steps are required: (1) grain-grain segmentation, and (2) conformal meshing of grain contacts. We have described these steps in detail in [23], but for the sake of completeness we include here a brief description.

For the grain-grain segmentation we start from a direct binary thresholding on the micro-CT that classifies voxels as pore or solid. After this, we want to reclassify the solid voxels with an integer index that represents at which grain it belongs. For this purpose we use a class of algorithms refer as watershed methods used for separating touching objects in binary images [24]. This algorithm computes first a distance transform 3D image, where for each solid voxel, the value of the Euclidean distance to the nearest pore/solid interface is recorded. If this is considered as a topographic depth map, the deeper parts of the image are the center of the objects. A watershed classification considers each solid voxel by the center to which it will roll down when following this inverted distance transform topographic map. In the final grain segmented 3D image each grain voxel has the value of the corresponding grain index, while pore voxels are labelled as 0.

In order to achieve an initial static solution for the segmented grains, it is of great importance to create a conformal mesh at the grain-grain contacts. A conformal mesh indicates that there is neither separation nor overclosure between any two grains of contact. The labeled voxelized 3D image is transformed into an unstructured mesh representation, where elements of the same grain are suitable for FE simulation and the elements at each side of a contact between grains conform to each other perfectly, without voids or overlaps in the contact boundary [23]. We generate the meshing for all the grains together, while maintaining the indices representing segmented grains, which results in a conformal mesh at the grain-grain contact. We can choose to have two separate surfaces or one combined interface for the conformal mesh, which corresponds to two case scenarios of free or fixed grain-grain contacts.

Finally, the meshed model is input into the finite element solver with prescribed strains/stress boundary conditions and grain-grain contact models [25,26]. A general parametrization of the cohesive contact model is used to capture contact behaviors of different levels of grain consolidation including two extreme scenarios: free grains, where only friction is modeled between grains, and fixed grains, where grains are completely fused. In terms of the FE simulations, the free grain contacts introduce duplicate nodes and elements that allows grain relocation whereas the fixed grain contacts model the solid framework as a whole.

2.1. Cohesive contact model

The concept of "bonded grains" has been widely adopted in discrete element method (DEM), which simulates each individual grain as a discrete rigid body [27–29]. Similarly, the FE simulations can simulate the bonded grain interface based on the cohesive contact model, with or without the possibility of damage and failure of the bond (Figure 1a). The cohesive constitutive laws include the linear elastic traction-separation model, damage initiation criterion, and damage evolution laws, which allow a precise description of the contact behavior. This work does not explicitly model the cement volume. Some processes, such as mineral segmentation, cement material property characterization, and grain meshing for cement phase, need to be developed to understand the effect of cement relative volume. We present an overview of the contact model, more details can be found in the FE solver documentation [26,30].

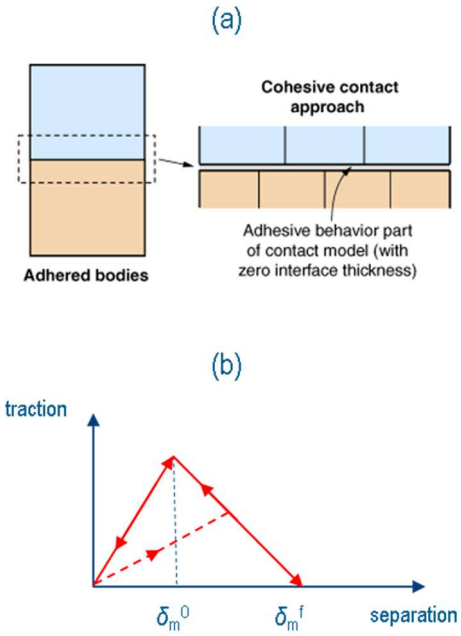

Fig. 1. (a) Schematic of cohesive contact behaviour [26]. (b) Typical traction-separation response.

The model assumes the traction-separation behavior initially linear elastic followed by the damage initiation and evolution. The elastic matrix K relates the normal and shear stresses to the normal and shear separations:

$$\begin{bmatrix} t_R \\ t_S \end{bmatrix} = \begin{bmatrix} K_{RR} & 0 \\ 0 & K_{SS} \end{bmatrix} \begin{bmatrix} \delta_R \\ \delta_S \end{bmatrix} \quad (1)$$

where t_R and t_S represent the traction stress components in normal and shear directions, δ_R and δ_S represent the corresponding separations. Normal compressive stress follows the usual contact behavior. The damage modeling consists of a damage initiation criterion and a damage evolution law. Damage initiation begins when the separations satisfy the specified initiation criteria:

$$max\left\{\frac{\delta_R}{\delta_R^0}, \frac{\delta_S}{\delta_S^0}\right\} = 1 \quad (2)$$

where $\delta_R{}^0$ and $\delta_S{}^0$ are critical separations in normal and shear directions. Note that purely compressive stress (negative value) does not result in damage. The damage evolution law

describes the degradation rate of the contact stiffness once the damage initiation starts. The contact stresses follow:

$$t_R = (1 - D)\bar{t}_R \quad (3)$$

$$t_S = (1 - D)\bar{t}_S \quad (4)$$

where D is the damage variable, $\bar{t}_R$ and $\bar{t}_S$ are contact stresses predicted by the elastic behavior (Eq. (1)) without damage. The damage variable D changes from 0 to 1 as the damage initiates and evolves and can be specified as a linear function of the effective separation δ_m. δ_m^f and δ_m^0 are the effective separation at complete failure and damage initiation, respectively. δ_m^{max} refers to the maximum value of the effective separation attained during the loading history. Figure 1b shows a typical traction-separation response for the cohesive contact model. Unloading subsequent to damage initiation is assumed to follow the history traction-separation path. Therefore, the cohesive contacts remain elastic until a bond failure occurs.

$$D = \frac{\delta_m^f(\delta_m^{max} - \delta_m^0)}{\delta_m^{max}(\delta_m^f - \delta_m^0)} \quad (5)$$

$$\delta_m = \sqrt{\delta_R^2 + 2\delta_S^2} \quad (6)$$

2.2 General parameterization

We describe in more detail the proposed new general parameterization of cohesive contact model that can capture both extreme contact behaviors: free grains and fixed grains, as well as any intermediate degree of grain consolidation.

The parameters of the contact model include the stiffness K_{RR} and K_{SS} for the linear elastic behavior, the critical separation δ_R^0 and δ_S^0, and the effective separation at complete failure δ_m^f for the damage behavior. In order to simplify the representation, we assume $K_{RR} = K_{SS} = K$, $\delta_R^0 = \delta_S^0 = \delta^0$, $\delta_m^f = 2.5 \times \delta_m^0$ to reduce the number of parameters. The stiffness K needs to be pre-determined and can be automatically computed such that the cohesive contact model of a very large δ^0 can reproduce the mechanical behavior of a solid framework with no grain contacts involved (i.e. fixed grain-grain contacts). Therefore, the cohesive contact model has only one adjustable parameter, the critical separation δ^0, which can be recast into a parametric relationship that represents the consolidation level as a function of a new parameter C.

We propose the following relationship between the critical separation δ^0 and the consolidation level, new parameter C, as follows:

$$\delta^0 = \Delta x \frac{C}{1 - C} \quad (7)$$

where Δx is a characteristic length for the granular system (with the same unit of δ^0), C is dimensionless and can change from 0 to 1 with an increasing level of consolidation. Eq. (7) indicates that $\delta^0 = \infty$ when $C = 1$ and $\delta^0 = 0$ when $C = 0$, representing two extreme scenarios of fixed and free grain-grain contacts. Figure 2 shows the traction-separation responses of various consolidation levels. A characteristic length is a global variable that can be estimated for instance from the grain size distribution, or grain-grain contact area distribution, as extracted from the 3D image itself.

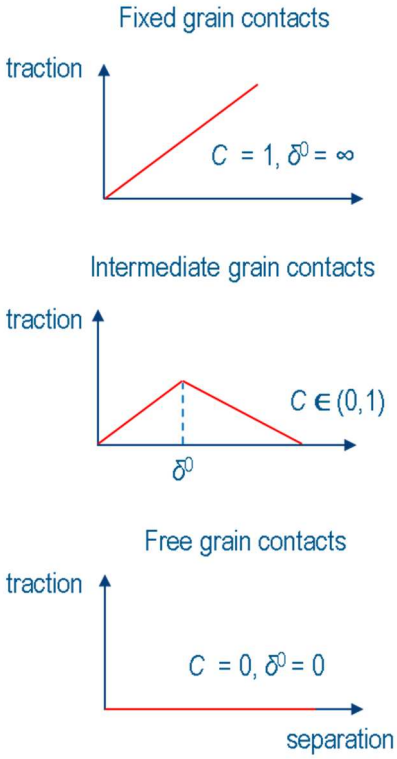

Fig. 2. Traction-separation responses of various consolidation levels (quantified by parameter C).

This single model can capture contact behaviors for different levels of grain consolidation. With this parametric cohesive contact model, we can simulate a wide range of sedimentary rocks, from unconsolidated (free grain contacts) to intermediate-consolidated rocks to well-consolidated rocks (fixed grain contacts).

2.3 Model validation

In order to validate this proposed simplification, first we test the parametric cohesive contact model through a simple scenario of three-grain packing. The grains are extracted from a micro-CT image of Fontainebleau sandstone model [31]. Figure 3a shows the grain mesh used in the FE simulation.

We fix the bottom of the packing and apply either a tensile or compressive stress on the top, i.e. tensile or compressive testing. The characteristic length Δx is assumed as 0.5 μm. Figure 3b shows the tensile testing results from simulations of the cohesive contact model with different consolidation levels C, and fixed and free grain contacts (no cohesive contacts applied). The results indicate that the parametric cohesive contact model can reproduce the fixed and free grain contact behaviors when $C = 1$ and $C = 0$, respectively. When $C = 0$, the grains will be readily separated by the tensile stress. When $C = 1$, the three grains behave as a solid framework with no grain separation. When C = 0.5, the tensile force shows an increase followed by a decrease due to the damage initiates, similar to Figure 2.

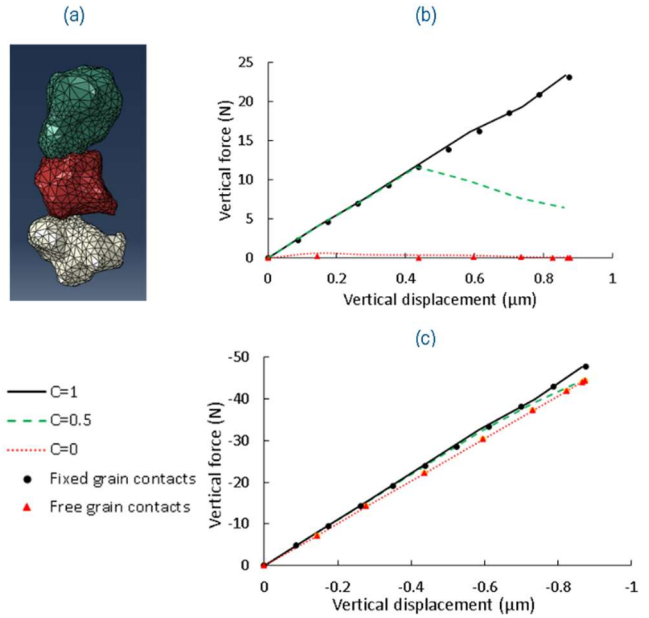

Fig. 3. (a) Grain mesh of a three-grain packing. Grains are differentiated by colors. Force-displacement results of (b) tensile testing, and (c) compressive testing. Parametric cohesive contact model can reproduce the fixed and free grain contact behaviors by changing the consolidation level *C*.

Figure 3c shows the simulation results of compressive testing. The compressive forces are with negative values to indicate the compaction. The parametric cohesive contact model can reproduce the fixed and free grain contact behaviors when $C = 1$ and $C = 0$, respectively. When $C = 0.5$, the force-displacement curve exhibits a transition from fixed grain contacts to free grain contacts because only two bonded contacts exist in the packing. The collective force-displacement behavior of a larger number of bonds appears to become linear as shown in the following section.

3 Results and discussion

We apply this new parametric cohesive contact model to three rock sample models including a sphere packing, a Grosmont Carbonate and a Fontainebleau Sandstone, each of it exhibiting different grain-grain contact behaviour. We measure the static elastic modulus by modelling the deformation of rock sample, rather than the dynamic elastic modulus (e.g. acoustic velocities). The dynamic elastic modulus is typically higher than the static modulus, and the values diverge significantly in rocks with a low elastic modulus [32,33]. We also present simulation results of a failure test on the Fontainebleau Sandstone model to demonstrate the impact of properly capturing the degree of consolidation on the rock strength and failure pattern.

3.1 Free grain contacts

A sphere packing is a very good example of free grain-grain contact behavior, where grain contacts are introduced duplicate nodes and elements that allows grain relocation. Sain (2010) generated the micro-CT image of a sphere packing (as shown in Figure 4a) and obtained its bulk and shear modulus as 1.17 GPa and 1.22 GPa through granular dynamic simulations [34]. The granular dynamic simulations can yield very similar elastic moduli as laboratory experiments on glass beads packs, dry Ottawa sands and dry Galveston sand [34–36]. Andrä et al. (2013) compared their numerical simulations directly based on image voxels (i.e. only allowing fixed grain-grain contacts) with the granular dynamic simulations and found a significant deviation [2]. On the contrary, our micromechanical finite element model allows grain relocation (i.e. free grain-grain contacts) therefore resulting in a very close modulus as the reference data in [34].

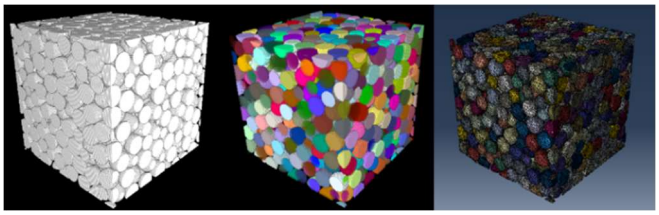

Fig. 4. From left to right: the original binary micro-CT image of sphere packing, segmented grains indicated by different colors, grain mesh for the FE solver.

Using this sphere pack model we demonstrate that the parametric cohesive contact model can mimic the free grain contacts. Following reference [2,23], we use a material property of quartz for the sphere packing: density is 2.65 g/cm^3, bulk modulus is 37.0 GPa, and shear modulus is 44.0 GPa. Table 1 summarizes the specifications for the sphere pack model.

Table 1. Specifications of the sphere packing.

Rock type	Sphere packing
Sample size (voxels)	398x319x398
Voxel size (μm)	14
Porosity	34.3%
Number of nodes	693,635
Number of elements	3,306,874

The parametric cohesive contact model has two parameters: the consolidation level *C* and the stiffness *K*. The consolidation level *C* is equal to 0 for free grain contacts. The stiffness *K* is calibrated to reproduce the mechanical behavior of fixed grain contacts. We perform hydrostatic compression test to measure the bulk modulus and shear test to measure the shear modulus. Table 2 summarizes the results. The parametric cohesive contact model with $C = 0$ yields very similar moduli as the free grain contacts from our previous work [23]. The results are not expected to be identical considering that the numerical simulations are based on different contact mechanisms.

Table 2. Bulk and shear moduli of sphere packing.

	Bulk modulus (GPa)	**Shear modulus (GPa)**
Cohesive contact model with $C = 0$	1.29	1.57
Free grain contacts	1.34	1.62
Difference	3.7%	3.1%

3.2 Fixed grain contacts

The Grosmont Carbonate was deposited around 380 million years ago in the late Devonian period in an open shallow limestone marine shelf environment [37]. The formation is composed of limestone and dolomite with minor amount of siltstone and shale. Grosmont Carbonate is a good example of fixed grain-grain contact behaviour, given the fact that Carbonates are typically recrystallized due to diagenetic processes. Therefore, all the grains behave as one solid framework. In this section, we perform the grain segmentation to demonstrate that cohesive contacts can mimic the behaviour of fixed grain contacts when C = 1. Please note that watershed grain segmentation is typically not applicable to complex carbonate structure. Such a segmentation is intended for validating the numerical asymptotic behaviour of the parametric cohesive contact model, but not necessarily indicates a real grain contact behaviour.

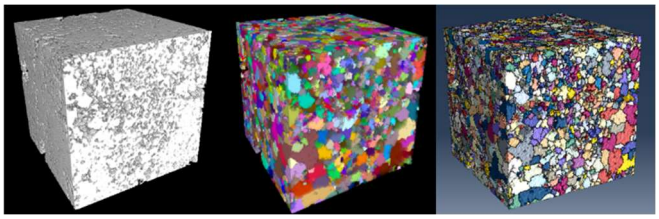

Fig. 5. From left to right: the original binary micro-CT image of Grosmont Carbonate, segmented grains indicated by different colors, grain mesh for the FE solver (only exterior edges are shown for better visualization).

Table 3 summarizes the specifications for the Grosmont Carbonate model. Following reference [22], we use a material property of 50% calcite and 50% dolomite for the Grosmont Carbonate: density is 2.79 g/cm^3, bulk modulus is 81.6 GPa, and shear modulus is 36.7 GPa. The consolidation level C is equal to 1 for fixed grain contacts and the stiffness K is the calibrated parameter. Table 4 shows the comparative results with our previous simulation for this model, and show that the parametric cohesive contact model with $C = 1$ gives very similar elastic moduli as the fixed grain contacts.

Table 3. Specifications of the Grosmont Carbonate.

Rock type	**Grosmont Carbonate**
Sample size (voxels)	400x400x400
Voxel size (μm)	2.02
Porosity	24.7%
Number of nodes	11,416,848
Number of elements	50,105,905

Table 4. Bulk and shear moduli of Grosmont Carbonate.

	Bulk modulus (GPa)	**Shear modulus (GPa)**
Cohesive contact model with $C = 1$	23.8	13.6
Fixed grain contacts	24.0	13.4
Difference	0.8%	1.5%

3.3 Various consolidation levels

Many sedimentary rock samples may exhibit different levels of consolidation as sediments are compacted and cemented under various geomechanical and geochemical conditions. In this section we focus on an intermediate consolidated rock, a Fontainebleau Sandstone.

For illustration purposes, we firstly apply the parametric cohesive contact model to a Fontainebleau model [31,38], with a relatively small volume of 100x100x100 voxels, and voxel size of 7.3 μm. Figure 6 shows the binary voxelized image, segmented grains, and conformal grain mesh used in the FE solver. Following reference [22], the material properties assigned are for quartz as in the sphere packing case.

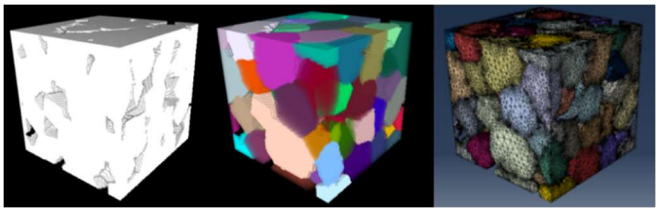

Fig. 6. From left to right: the original binary micro-CT image of Fontainebleau model, segmented grains indicated by different colors, and grain mesh for the FE solver.

We perform uniaxial strain tests on this Fontainebleau model, which requires an incremental strain in the vertical direction and zero strains in the horizontal directions [23]. Figure 7a shows stress-strain behaviours of various consolidation level C. When $C = 0$ and $C = 1$, the cohesive contact model can reproduce the moduli of free and fixed grain contacts, respectively. The modulus shows an increase as the consolidation level C increases. Figure 7b shows the normalized modulus as a function of the consolidation level. The modulus tends to become asymptotic approaching to the

two ends. We find that the data can be fitted well by a logistic function:

$$f(x) = \frac{1}{1+e^{-k(x-x_0)}} \quad (8)$$

where the fitted parameters k and x_0 are 10.0 and 0.5, respectively. The purpose of using a fitting function is to minimize the number of simulations needed to create a complete contact model valid for all range of consolidation levels $0 \leq C \leq 1$ behavior. We found that we only need to run two more simulations apart from the two end-member simulations ($C = 0$ and $C = 1$) to completely capture the effect of consolidation level.

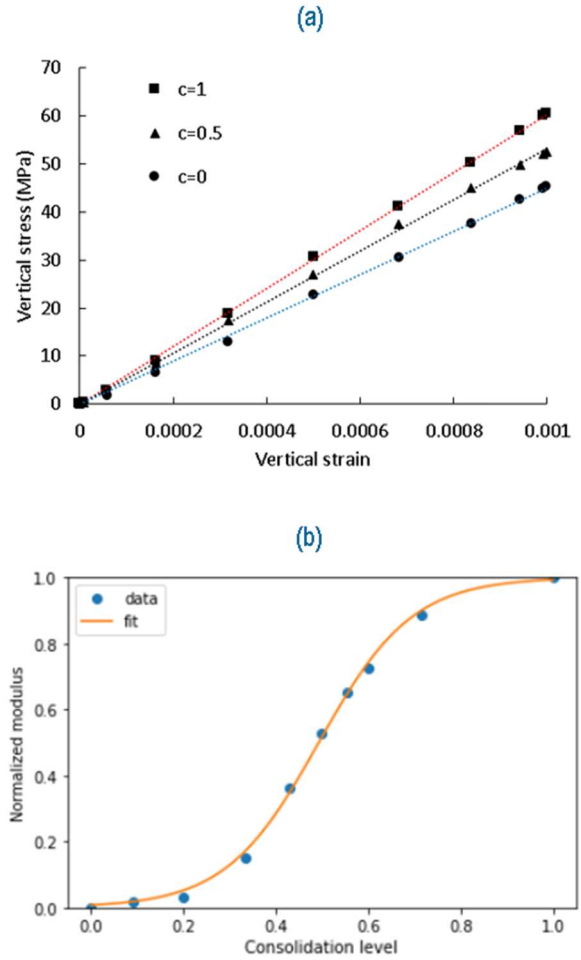

Fig. 7. (a) Stress-strain response for various consolidation levels C. (b) Normalized modulus as a function of consolidation level. The result can be fitted by a logistic function.

With the knowledge obtained from simulations on the small Fontainebleau model, we further apply the parametric cohesive contact model to a larger Fontainebleau Sandstone micro-CT model of 288x288x300 voxels [2]. The voxel size is 7.5 μm. The sample porosity is 14.7%. The material properties are assigned as quartz. Figure 8 shows the voxelized image, segmented grains, and conformal grain mesh.

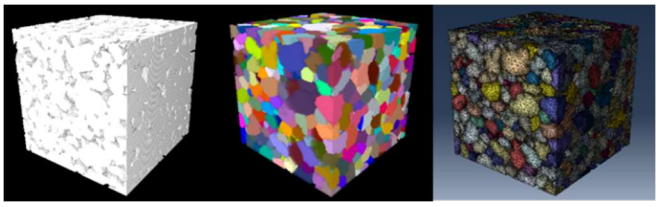

Fig. 8. From left to right: the original binary micro-CT image of Fontainebleau sandstone, segmented grains, and grain mesh.

We perform a hydrostatic compression test to measure the bulk modulus. Figure 9a shows the stress-strain behaviours for various consolidation levels C. The parametric cohesive contact model can reproduce the moduli of fixed and free grain contacts when $C = 1$ and $C = 0$, respectively. Two intermediate consolidation levels result in a modulus in between. The parameters k and x_0 of our logistic fitting function are 15.9 and 0.5, respectively.

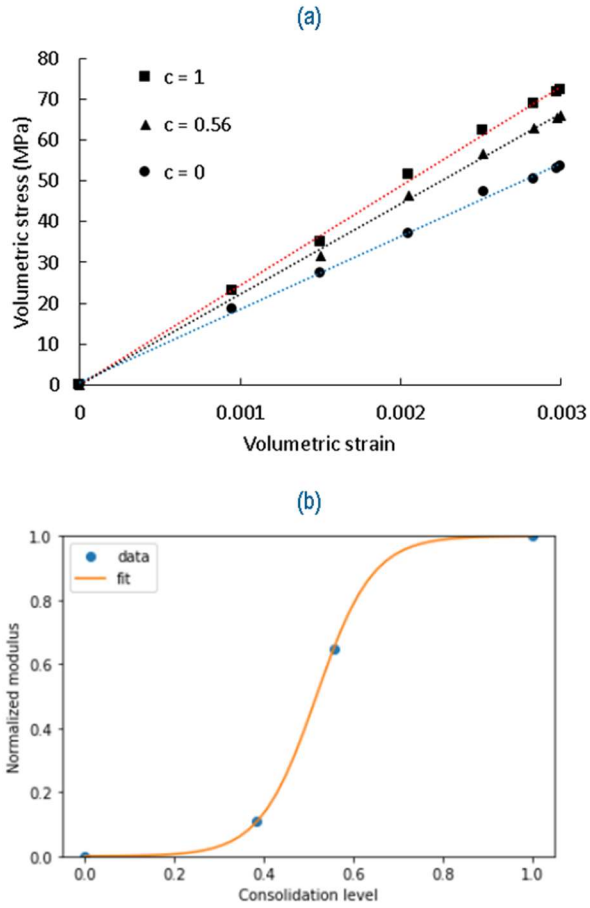

Fig. 9. (a) Stress-strain response for various consolidation levels C. (b) Normalized modulus as a function of consolidation level. The result can be fitted by a logistic function.

The experimentally measured bulk modulus is ~22.2 GPa, which corresponds to a consolidation level C of 0.56 based on the simulation results in Figure 9 [2]. We further perform a shear test to measure the shear modulus when $C = 0.56$. We obtain a shear modulus of 24.9 GPa, which is also close to the laboratory-measured shear modulus. Therefore, this method can be used to estimate the contact consolidation level by finding the C value so that the experiments match with simulations on a corresponding micro-CT image. The

model also allows the users to select the consolidation level as an input parameter based on their knowledge of diagenesis history of sedimentary rock samples. Some ideas have been discussed about relating the consolidation level with the relative size of the grain-grain contact areas relative to the grain sizes. Small relative contact areas should correspond to lower consolidation levels, while larger relative contact areas should correspond to higher consolidation levels. A systematic study with a representative population of rock types and consolidation levels using the new parametric cohesive contact model should provide some validation of this idea.

Table 5. Bulk and shear moduli of Fontainebleau Sandstone.

	Bulk modulus (GPa)	**Shear modulus (GPa)**
Experimental result	22.2	23.5
Numerical result ($C = 0.56$)	22.2	24.9
Difference	0.0%	5.9%

3.4 Failure test

The rock failure behaviour manifests the significance to capture well the consolidation level. Uniaxial compression tests are widely used to determine the uniaxial compressive strength (UCS) and deformability of rock samples [39,40]. The testing sample is loaded in the axial direction with no confinement in the radial directions. The ratio of height/diameter of the samples is typically between 2 and 3 [41]. A ratio smaller than 2 will result in high uniaxial compressive strength [42].

In this section, we perform uniaxial compression tests on a cylindrical volume from the Fontainebleau model used in the previous section, at various consolidation levels C. All the other model parameters remain invariant. The sample has a height of 500 voxels and a diameter of 250 voxels. The voxel size is 7.3 μm. Figure 10 shows the voxelized image of segmented grains and the corresponding grain mesh used in the FE simulations of uniaxial compression test.

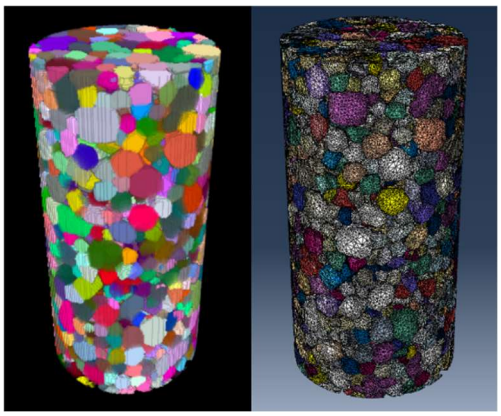

Fig. 10. (Left) Voxelized image of segmented grains. (Right) Grain meshing for FE simulation of failure test.

Figure 11 shows the evolution of vertical displacement field as the sample is being compressed in the vertical direction (C = 0.2). The Fontainebleau sample is initially intact and finally ruptures with a shear band. Figure 12 shows the vertical stress as a function of vertical strain for various consolidation levels C. When C = 1, the grains are fused together and the sample behaves elastic with an infinite strength. When C = 0, the grains are unconsolidated and the sample fails when the vertical stress reaches the uniaxial compressive strength, with friction as the only remaining force. An intermediate C will result in stress-strain curves in between the two end-member scenarios. When C is relatively small (e.g. $C = 0.2$), the stress-strain curve is very close to the result of C = 0 due to the asymptotic nature of Eq. (7), and shown in Figures 7b and 9b. The simulation results show that the rock failure behaviour is conditioned by the consolidation level, which is parameterized into the cohesive contact model in this work.

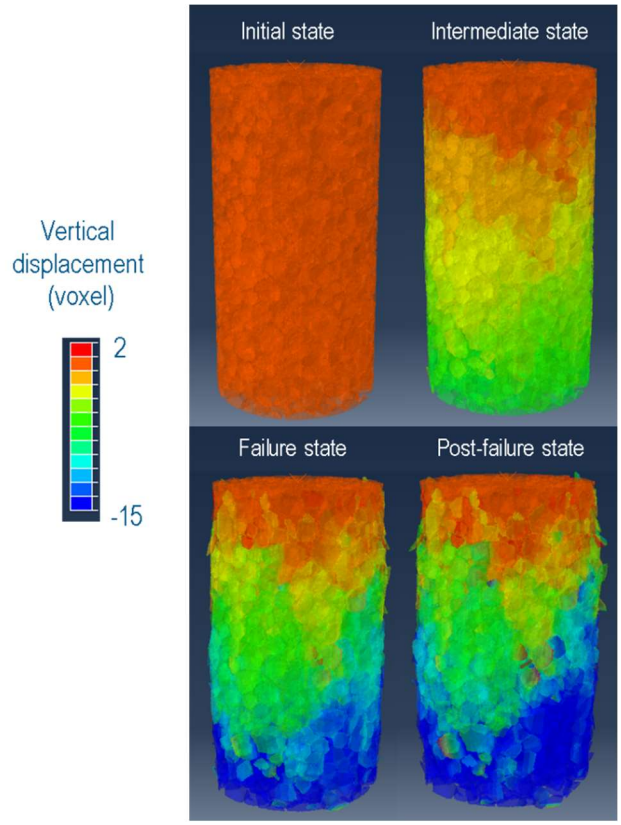

Fig. 11. Evolution of vertical displacement field as the Fontainebleau model is compressed in the vertical direction. The grains are shown semi-transparent for a better visualization. The sample ruptures with a shear band at the failure state.

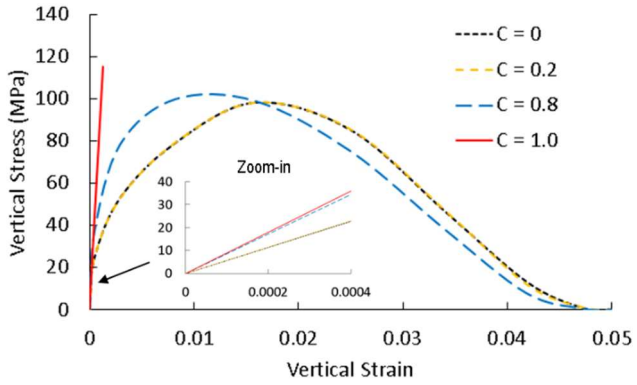

Fig. 12. Vertical stress as a function of vertical strain for various consolidation levels *C*. A larger C results in a larger uniaxial strength and elastic modulus.

Table 6 summarizes the Young's modulus and uniaxial compressive strength based on the results shown in Figure 12. A larger consolidation level parameter *C* will result in a larger Young's modulus and uniaxial compressive strength. Han (1987) experimentally measured the Young's modulus of several Fontainebleau sandstones and the results range from 36 to 79 GPa [43]. Baud et al. (2014) experimentally measured the uniaxial compressive strength of several Fontainebleau sandstones and the results were from 44 to 122 MPa [44]. Our numerical simulations for this particular Fontainebleau model yield reasonable values of Young's modulus and uniaxial compressive strength compared to these reference experimental data.

In addition to the consolidation level, the contact friction is another critical parameter to the rock failure process. We adopt the Coulomb friction model which relates the maximum allowable frictional stress across a grain contact to the contact pressure between the grains. The critical frictional stress at which sliding of the contacts starts is proportional to the product of friction coefficient and contact pressure. We assume a friction coefficient of 0.2 throughout this study. Besides, we find that (1) the elastic-plastic transition is smooth compared to many real loading scenarios, and (2) the post-peak behaviour is less catastrophic than real failures. This may be a result of the fact that the current meshing process is not ideal and introduces non-smooth contact boundaries that can add friction to grain contacts. The future work will be improving the grain meshing process to allow smooth contact boundaries that facilitate relative large-strain grain relocation.

Table 6. Bulk and shear moduli of Fontainebleau Sandstone.

	Young's modulus (GPa)	**Uniaxial compressive strength (MPa)**
$C = 0$	57.0	98.2
$C = 0.2$	57.4	98.3
$C = 0.8$	86.1	102.6
$C = 1.0$	89.8	infinity

4 Concluding remarks

In this paper, we extend our previous micromechanics workflow described in [23] to a parametric cohesive contact model. The presented workflow can capture both extreme contact behaviors: free grains and fixed grains, as well as any intermediate degree of grain consolidation. We present a benchmark study on several samples and compare with laboratory-measured elastic moduli to estimate its degree of consolidation. Simulations that do not include the grain contact modeling, tend to overestimate the elastic moduli, which manifests the significance of our contribution to capture well the grain contact behavior. To demonstrate the impact of properly capturing the degree of consolidation on the rock strength and failure pattern, we present results for numerical uniaxial compression testing consistent with measured results. This workflow provides a physics-based solution to the complex grain-grain contact behavior, which complements laboratory core analysis, and can be useful to reveal underlying grain-scale processes governing rock mechanical behavior. The importance of a more complete microscopic understanding of core-scale mechanical properties is ultimately reflected in the quality of the inputs that we use for our up-scaled geomechanics models, as well as enabling a more comprehensive framework for digital rock simulated petrophysical properties at different NCS conditions.

5 Nomenclature

Notation
K = stiffness
t = traction stress
δ = separation in normal direction
D = damage variable
C = consolidation level
Δx = characteristic length
k , x_0 = fitting parameters for logistic function

Subscripts
R = normal direction
S = shear direction
m = effective property

Superscripts
f = failure condition
0 = critical condition
max = maximum value

Acknowledgments

We would like to acknowledge the support of Dassault Systèmes to allow the publication of this work.

References

[1] H. Andrä, N. Combaret, J. Dvorkin, E. Glatt, J. Han, M. Kabel, Y. Keehm, F. Krzikalla, M. Lee, and C. Madonna, *Digital Rock Physics Benchmarks—Part I: Imaging and Segmentation*, Comput. Geosci. **50**, 25 (2013).

[2] H. Andrä, N. Combaret, J. Dvorkin, E. Glatt, J. Han, M. Kabel, Y. Keehm, F. Krzikalla, M. Lee, and C. Madonna, *Digital Rock Physics Benchmarks—Part II: Computing Effective Properties*, Comput. Geosci. **50**, 33 (2013).

[3] R. Xu, B. Crouse, D. M. Freed, A. Fager, G. R. Jerauld, N. Lane, and Q. Sheng, *Continuous vs Discontinuous Capillary Desaturation and Implications for IOR/EOR*, in *Paper SCA2018-066 Presented at at the International Symposium of the Society of Core Analysts Held in Trondheim, Norway* (2018).

[4] B. Crouse, D. M. Freed, N. Koliha, G. Balasubramanian, R. Satti, D. Bale, and S. Zuklic, *A Lattice-Boltzmann Based Method Applied to Digital Rock Characterization of Perforation Tunnel Damage*, in *Paper SCA2016-058 Presented at the International Symposium of the Society of Core Analysts Held in Snow Mass, Colorado, USA* (2016).

[5] M. J. Blunt, *Flow in Porous Media—Pore-Network Models and Multiphase Flow*, Curr. Opin. Colloid Interface Sci. **6**, 197 (2001).

[6] J. Dvorkin, M. Armbruster, C. Baldwin, Q. Fang, N. Derzhi, C. Gomez, B. Nur, and A. Nur, *The Future of Rock Physics: Computational Methods vs. Lab Testing*, First Break **26**, (2008).

[7] C. H. Arns, M. A. Knackstedt, M. V. Pinczewski, and W. B. Lindquist, *Accurate Estimation of Transport Properties from Microtomographic Images*, Geophys. Res. Lett. **28**, 3361 (2001).

[8] M. Andrew, H. Menke, M. J. Blunt, and B. Bijeljic, *The Imaging of Dynamic Multiphase Fluid Flow Using Synchrotron-Based X-Ray Microtomography at Reservoir Conditions*, Transp. Porous Media **110**, 1 (2015).

[9] A. K. Turner, F. H. Kim, D. Penumadu, and E. B. Herbold, *Meso-Scale Framework for Modeling Granular Material Using Computed Tomography*, Comput. Geotech. **76**, 140 (2016).

[10] C. H. Arns, M. A. Knackstedt, W. V. Pinczewski, and E. J. Garboczi, *Computation of Linear Elastic Properties from Microtomographic Images: Methodology and Agreement between Theory and Experiment*, Geophysics **67**, 1396 (2002).

[11] T. W. J. De Geus, J. Vondřejc, J. Zeman, R. H. J. Peerlings, and M. G. D. Geers, *Finite Strain FFT-Based Non-Linear Solvers Made Simple*, Comput. Methods Appl. Mech. Eng. **318**, 412 (2017).

[12] M. M. Hossain, J. Arns, Z. Liang, Z. Chen, and C. H. Arns, *Humidity Effects on Effective Elastic Properties of Rock: An Integrated Experimental and Numerical Study*, J. Geophys. Res. Solid Earth **124**, 7771 (2019).

[13] M. A. Knackstedt, C. H. Arns, and W. V. Pinczewski, *Velocity-Porosity Relationships, 1: Accurate Velocity Model for Clean Consolidated Sandstones*, Geophysics **68**, 1822 (2003).

[14] B. Crouse, S. Gill, J. Bautista, G. Balasubramanian, and D. Freed, *Digital Prediction of Porosity and Permeability Variation of Unconsolidated Sands Caused by Over-Burden Pressure*, in *NAFEMS World Congress* (2019).

[15] A. B. Andhumoudine, X. Nie, Q. Zhou, J. Yu, O. I. Kane, L. Jin, and R. R. Djaroun, *Investigation of Coal Elastic Properties Based on Digital Core Technology and Finite Element Method*, Adv. Geo-Energy Res. **5**, 53 (2021).

[16] S. Boggs Jr, *Principles of Sedimentology and Stratigraphy* (Pearson Education, 2014).

[17] E. J. Garboczi and J. G. Berryman, *Elastic Moduli of a Material Containing Composite Inclusions: Effective Medium Theory and Finite Element Computations*, Mech. Mater. **33**, 455 (2001).

[18] S. Meille and E. J. Garboczi, *Linear Elastic Properties of 2D and 3D Models of Porous Materials Made from Elongated Objects*, Model. Simul. Mater. Sci. Eng. **9**, 371 (2001).

[19] E. H. Saenger, *Numerical Methods to Determine Effective Elastic Properties*, Int. J. Eng. Sci. **46**, 598 (2008).

[20] C. H. Arns, M. Madadi, A. P. Sheppard, and M. A. Knackstedt, *Linear Elastic Properties of Granular Rocks Derived from X-Ray-CT Images*, in *SEG Technical Program Expanded Abstracts 2007* (Society of Exploration Geophysicists, 2007), pp. 1711–1715.

[21] N. Saxena, R. Hofmann, A. Hows, E. H. Saenger, L. Duranti, J. Stefani, A. Wiegmann, A. Kerimov, and M. Kabel, *Rock Compressibility from Microcomputed Tomography Images: Controls on Digital Rock Simulations*, Geophysics **84**, WA127 (2019).

[22] J. Fredrich, N. Lane, and J. Toms, *Image-Based Direct Numerical Simulation of Petrophysical Properties under Simulated Stress and Strain Conditions*, U.S. Patent 9,348,056 (24 May 2016).

[23] Z. Sun, R. Salazar-Tio, L. Duranti, B. Crouse, A. Fager, and G. Balasubramanian, *Prediction of Rock Elastic Moduli Based on a Micromechanical Finite Element Model*, Comput. Geotech. **135**, 104149 (2021).

[24] D. Legland, I. Arganda-Carreras, and P. Andrey, *MorphoLibJ: Integrated Library and Plugins for Mathematical Morphology with ImageJ*, Bioinformatics **32**, 3532 (2016).

[25] S. Qin, R. McLendon, V. Oancea, and A. M. Beese, *Micromechanics of Multiaxial Plasticity of DP600: Experiments and Microstructural Deformation Modeling*, Mater. Sci. Eng. A **721**, 168 (2018).

[26] Abaqus, *Abaqus 6.10 Online Documentation*, Abaqus User Subroutines Ref. Man. (2010).

[27] M. Obermayr, K. Dressler, C. Vrettos, and P. Eberhard, *A Bonded-Particle Model for Cemented Sand*, Comput. Geotech. **49**, 299 (2013).

[28] D. O. Potyondy and P. A. Cundall, *A Bonded-Particle Model for Rock*, Int. J. Rock Mech. Min. Sci. **41**, 1329 (2004).

[29] Z. Sun, D. N. Espinoza, and M. T. Balhoff, *Discrete Element Modeling of Indentation Tests to Investigate Mechanisms of CO2 -Related Chemo-Mechanical Rock Alteration*, J. Geophys. Res. Solid Earth **121**, 7867 (2016).

[30] H. Harkness, G. Ang, P. Vijalapura, and D. Cojocaru, *Contact Stress Accuracy with Robust and Broadly Applicable Implicit Contact Algorithm*, in *NWC (Nafems World Congress)* (2011).

[31] F. D. E. Latief, B. Biswal, U. Fauzi, and R. Hilfer, *Continuum Reconstruction of the Pore Scale Microstructure for Fontainebleau Sandstone*, Phys. A Stat. Mech. Its Appl. **389**, 1607 (2010).

[32] V. Brotons, R. Tomás, S. Ivorra, A. Grediaga, J. Martínez-Martínez, D. Benavente, and M. Gómez-Heras, *Improved Correlation between the Static and Dynamic Elastic Modulus of Different Types of Rocks*, Mater. Struct. **49**, 3021 (2016).

[33] J. M. Ide, *Comparison of Statically and Dynamically Determined Young's Modulus of Rocks*, Proc. Natl. Acad. Sci. U. S. A. **22**, 81 (1936).

[34] R. Sain, *Numerical Simulation of Pore-Scale Heterogeneity and Its Effects on Elastic, Electrical and Transport Properties* (Stanford University, 2010).

[35] S. N. Domenico, *Elastic Properties of Unconsolidated Porous Sand Reservoirs*, Geophysics **42**, 1339 (1977).

[36] M. A. Zimmer, *Seismic Velocities in Unconsolidated Sands: Measurements of Pressure, Sorting, and Compaction Effects* (Stanford University, 2004).

[37] B. E. Buschkuehle, F. J. Hein, and M. Grobe, *An Overview of the Geology of the Upper Devonian Grosmont Carbonate Bitumen Deposit, Northern Alberta, Canada*, Nat. Resour. Res. **16**, 3 (2007).

[38] R. Hilfer and T. Zauner, *High-Precision Synthetic Computed Tomography of Reconstructed Porous Media*, Phys. Rev. E **84**, 62301 (2011).

[39] C. E. Fairhurst and J. A. Hudson, *Draft ISRM Suggested Method for the Complete Stress-Strain Curve for Intact Rock in Uniaxial Compression*, Int. J. Rock Mech. Min. Sci. **36**, 279 (1999).

[40] Z. T. Bieniawski and M. J. Bernede, *Suggested Methods for Determining the Uniaxial Compressive Strength and Deformability of Rock Materials: Part 1. Suggested Method for Determining Deformability of Rock Materials in Uniaxial Compression*, in *International Journal of Rock Mechanics and Mining Sciences & Geomechanics Abstracts*, Vol. 16 (Elsevier, 1979), pp. 138–140.

[41] E. Tuncay and N. Hasancebi, *The Effect of Length to Diameter Ratio of Test Specimens on the Uniaxial Compressive Strength of Rock*, Bull. Eng. Geol. Environ. **68**, 491 (2009).

[42] A. B. Hawkins, *Aspects of Rock Strength*, Bull. Eng. Geol. Environ. **57**, 17 (1998).

[43] D.-H. Han, Effects of Porosity and Clay Content on Acoustic Properties of Sandstones and Unconsolidated Sediments, Stanford Univ., CA (USA), 1987.

[44] P. Baud, T. Wong, and W. Zhu, *Effects of Porosity and Crack Density on the Compressive Strength of Rocks*, Int. J. Rock Mech. Min. Sci. **67**, 202 (2014).